D2.2(MVIRI): Report on the MVIRI FCDR: Uncertainty

Frank Rüthrich (1), Emma Woolliams (2), Yves Govaerts (3), Ralf Quast (4), Jonathan Mittaz(2,5)

(1) EUMETSAT, (2) National Physical Laboratory, (3) Rayference, (4) FastOpt, (5) University of Reading

14th August 2017

FIDUCEO has received funding from the European Union's Horizon 2020 Programme for Research and Innovation, under Grant Agreement no. 638822

Contents

1 Introduction

1.1 Scope

This document is one of the five documents that make up the D2-2 report on “traceability chains for FCDRs”. Since the original project proposal our thoughts have refined and while this document describes the “sequence of measurement standards and calibrations that is used to relate a measurement result to a reference” (the VIM definition of a traceability chain), it is not presenting this in the form of a chain.

This document provides an overview of the uncertainty analysis for the analysed sensors along with the methods to establish metrological traceability for the developed FCDRs.

This document is specifically about the MVIRI FCDR. The document D2-2a provides an overview of the effects tables.

1.2 Version Control

Version	Reason	Reviewer	Date of Issue
1.a			
1.b			
1.c			

1.3 Applicable and Reference Documents

1.3.1 D2-2 set of documents

D2-2a	Principles behind the FCDR effects table
D2-2(microwave)	Report on the MW FCDR: Uncertainty
D2-2(HIRS)	Report on the HIRS FCDR: Uncertainty
D2-2(AVHRR)	Report on the AVHRR FCDR: Uncertainty
D2-2(MVIRI)	Report on the MVIRI FCDR: Uncertainty (This document)

1.3.2 References

P. Bretagnon; G. Francou (1988): "Planetary theories in rectangular and spherical variables. VSOP87 solutions". Astronomy & Astrophysics. ***202****: 309–315.*

Clark, Kliney and White (1997): Image Processing Software Detailed Design Document. Issue 2.2. EUMETSAT ref: MTP/BF/0901/SP/008

Keys (1981): Cubic Spline Interpolation for Digital Image Processing. IEEE ASSP Vol. 26 No. 6

Michel, Bleuez and Roche (1997): Meteosat Flight Operational Manual. EUMETSAT: MTP.88D.304

Nicodemus, F. E., J. C. Richmond, J. J. Hsia, I. W. Ginsberg, and T. Limperis. 1977: ‘Geometrical Considerations and Nomenclature for Reflectance’. National Bureau of Standards.

R. Quast and R. Giering (2016): WP4.1 Reconstruction of Meteosat Spectral Response Functions Project report, FIDUCEO project

R.Roebeling, V.O.John and F.Rüthrich (2017): WP4.1 Product User Guide MVIRI FCDR Pre-Beta Release, FIDUCEO project

J. Unzalu (1987): Deformation Matrix for Rectification of Meteosat Images. PROFS Database Reference: DRAFT4

1.4 Glossary

2 General overview

2.1 FIDUCEO effects tables

In FIDUCEO we have defined a standardized effects table which describes

- the uncertainty associated with a given effect
- the sensitivity coefficient required to propagate uncertainties associated with that effect to uncertainties associated with the measurand (Earth radiance, reflectance or brightness temperature)
- the correlation structure over spatial, temporal and spectral scales for errors from this effect

The concepts behind the effects tables are described in D2-2a. In this document we provide a discussion of the effects tables and uncertainty propagation for a single instrument series; here the MVIRI FCDR.

3 The MVIRI instrument

3.1 MVIRI on Meteosat

The Meteosat visible and infrared imager (MVIRI) is a radiometer that has been installed on all Meteosat spacecrafts of the first generation. The first satellite of this kind was launched in 1977, followed by a series of 6 successors. The orbit of the Meteosat satellites is geostationary and they were designed to provide one image of the earth every 30 minutes. Continuous data from the sub-satellite position of 0° are available since Meteosat 2, comprising now more than 24 years of data.

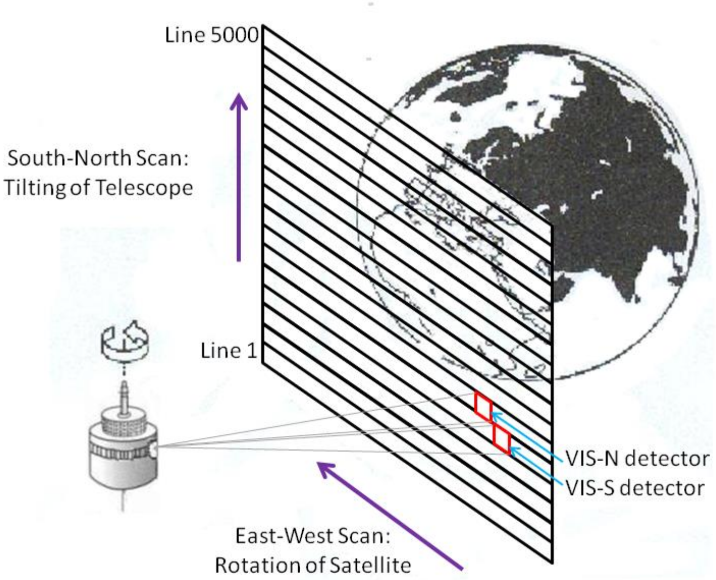

Figure 1: Scan concept of the MVIRI visible band on board the meteosat first generation spacecrafts. Own illustration, inspired by https://directory.eoportal.org/web/eoportal/satellite-missions/m/meteosat-second-generation.

The visible band of MVIRI essentially consists of 4 silicon photodiodes, 2 of which are active and 2 for backup, which respond to the light captured by the telescope. The position of the two active sensors is shifted relative to each other in north-south direction, so that they measure adjacent spots. Figure 1 shows the scan concept for the MVIRI visible band. Meteosat satellites are spin-stabilized and therefore, unlike other satellites, they do not need a rotating scan-mirror. VIS-Images result from the interplay of the detectors measuring, the satellite rotating at a defined speed and the telescope tilting to a defined angle. During one revolution of the satellite, each of the two active sensors acquires one scan-line across the earth. The two scan-lines are sent to the ground station during that part of the revolution, during which the radiometer is not directed towards the earth (Michel, Bleuez and Roche, 1997; p. 96). For the next revolution the sensor is tilted slightly northward, so that the following scan-lines follow up north of the previous ones.

The detection system consists of a telescope and silicon photodiodes and therefore responds to Earth radiance in the spectral range from ~300 nm to ~1100 nm. Before a scan-line is sent to earth, it is converted into a digital count value. This A/D conversion was done at 6 bits for the early Meteosat-2 and -3 satellites and at 8 bits for later satellites.

The preprocessing of the raw data from the transmitted scan lines (level 0) into geo-rectified level 1.5 data is necessary to compensate for image distortions that are due to satellite wobbling. The pixels of the raw count images are transferred into a rectified grid based on a deformation matrix (Unzalu, 1987) that is optimized for each image. Interpolation is done using Key's cubic convolution (Keys, 1981). This method uses a symmetric kernel over 4 pixels in each dimension. Thus, a total of 16 surrounding pixels determine the value of one pixel in the rectified grid. This is illustrated in Figure 2. The ideal location of the kernel that has to be used for each rectified pixel is determined based on the "ideal pixel" concept in the image processing software (Clark, Kliney and White, 1997; p 191,639). Interpolation is first performed in line-direction. Therefore third-order polynomials are fitted to each row of 4 raw-pixel values. The interpolated values from each row of the kernel are then interpolated in y-direction (Figure 2). The rectified grid then is populated with the truncated integer results of the interpolation.

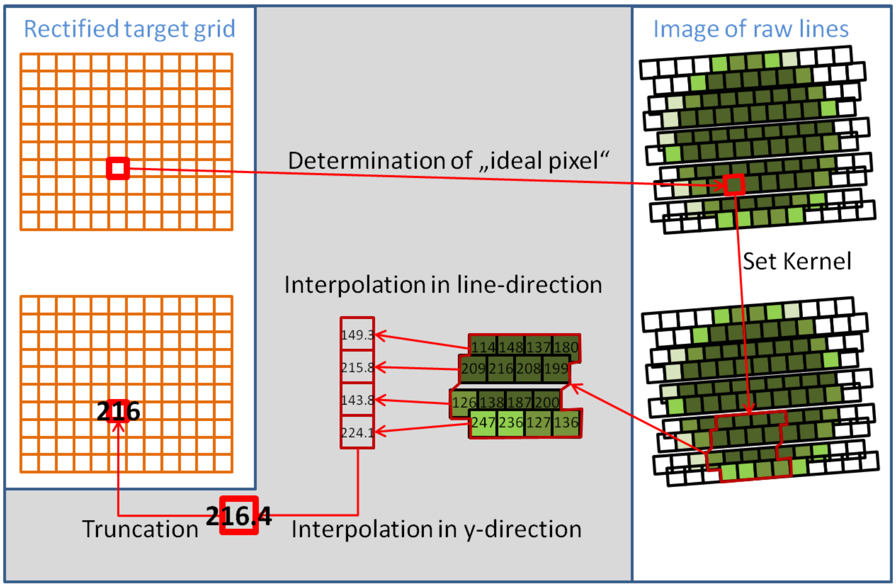

Figure 2: Flow chart on the rectification/interpolation algorithm as described in Keys (1981) and Clark, Kliney and White (1997) p 639. Example values are calculated using cubic spline interpolation with an assumed distance between rectified and ideal pixel of 0.1 pixels in both, x- and y-direction.

Corrections are also made, where necessary (Meteosat-3, -6) to correct for differences between the two different detectors. On the newer satellites (MET 3 onwards) the signal is dark corrected using the space-views in the four corners of the image.

MVIRI calibration is performed using calibration coefficients which express the relation between digital counts and corresponding radiance. To establish such a relation, in the absence of on-board calibration capability, reference top-of-atmosphere (TOA) radiances are necessary. These are obtained using radiative transfer modelling, combined with surface bidirectional reflectance function (BRDF) models, to derive modelled radiances above pre-defined bright desert and dark ocean target sites[1]. Atmospheric information required for these models is established using the latest set of ECMWF data, with aerosol type and total column ozone derived from monthly (NOAA) climatology tables. The modelled radiance above these sites is band integrated with the instrument spectral response function to establish a band-integrated TOA effective radiance.

This calibration can be determined at regular intervals throughout the sensor lifetime. The different individual calibrations are then used to establish a linear drift in the sensor calibration coefficient. The sensor calibration coefficient at any particular time is calculated from this drift function.

While MVIRI effectively measures the observed TOA radiance, the FCDR of interest is for band-integrated Bidirectional Reflectance Factor (BRF). The BRF is defined as the “ratio of the radiant flux actually reflected by a sample surface to that which would be reflected into the same reflected-beam geometry by an ideal (lossless) perfectly diffuse (lambertian) standard surface irradiated in exactly the same way as the sample.” (Nicodemus, 1977) This is calculated from the band-integrated radiance and the incident solar irradiance and the solar zenith angle.

---

[1] Within this project there is also work on the use of deep convective clouds as references.

3.2 The MVIRI measurement function

The MVIRI band-integrated BRF measurement function is given by:

$$\rho = \frac{\pi d^2}{\tilde{E}_{0,\mathrm{sun}} \cos\theta} \left[\left(\bar{C}_\mathrm{E} - \bar{C}_\mathrm{S} \right) \left(a_0 + a_1 D_t + 0 \right) \right]. \qquad \text{Eq 3-1}$$

The term $\pi d^2 / \left(\tilde{E}_{0,\mathrm{sun}} \cos\theta \right)$ represents the conversion from radiance (the instrument's native measurement quantity) to BRF. $\tilde{E}_0$ is the band integrated solar irradiance at one astronomical unit and d is the Earth-Sun distance in astronomical units, and θ is the solar zenith angle (see Section 3.2.1). The band-integrated solar irradiance is given by

$$\tilde{E}_{0,\mathrm{sun}} = \int \xi(\lambda;t) E_{0,\mathrm{sun}}(\lambda) \,\mathrm{d}\lambda \,. \qquad \text{Eq 3-2}$$

The rectified Earth counts,

$$\bar{C}_\mathrm{E} = \sum_j w_j C_{\mathrm{E},j} \qquad \text{Eq 3-3}$$

is calculated from a cubic spline, which acts as a local weighted sum of the measured Earth counts on neighbouring pixels (this is to perform the rectification, see Figure 2). The averaged space counts,

$$\bar{C}_\mathrm{S} = N_\mathrm{C}^{-1} \sum_{c=0}^{8} C_{\mathrm{S},c} \qquad \text{Eq 3-4}$$

is a mean of the space-view pixel count in the eight[2] "space corners" of the image. Note that both the rectified Earth counts and the averaged space counts combine measured values from both of the two detectors (see Figure 1).

The instrument gain (counts to radiance conversion) is given by $a_0 + a_1 D_t$ evaluated from the linear fit to the calibration events (see Section 3.2.2).

The zero represents the suitability of this measurement function (see Section 3.2.4).

3.2.1 Solar zenith angle

The solar zenith angle is determined from the latitude, longitude and the time of acquisition.

$$\theta = \cos^{-1}\left[\sin(\gamma)\sin(\varphi) + \cos(\gamma)\cos(h)\cos(\varphi) \right] \qquad \text{Eq 3-5}$$

where, γ is the solar declination (calculated from pixel acquisition time), φ is the latitude and h is the local hour angle (from pixel acquisition time and longitude).

---

[2] For each detector 4 „space corners" are available in the non-rectified images. The combined mean space corner count will thus be estimated from 8 corners.

3.2.2 Calibration coefficients

The calibration coefficients a_0, a_1 are determined from a time-series of observations and modelled band-integrated radiances over the target sites. From this time series, the coefficients are determined by fitting a straight line.

The individual calibration points (to which that straight line is fitted) are determined from two quantities – the measured signal (rectified Earth Counts minus averaged Space Counts) over the target site, and the modelled TOA band-integrated radiance over those sites.

The modelled TOA band-integrated spectral radiance for a pixel (i, j) at time t is obtained by spectrally integrating a hyperspectral TOA radiance model weighted by the normalised (to unit area) instrument spectral response function, thus:

$$\tilde{L}_{\mathrm{TOA};t,i,j} = \int_{\lambda_{\min}}^{\lambda_{\max}} \xi_t(\lambda;t) L\left(\lambda;\Omega_{t,i,j},\chi_{t,i,j}\right)\mathrm{d}\lambda \qquad \textit{Eq 3-6}$$

where, $\xi_t(\lambda;t)$ is the instrument spectral response function (at time t) and the modelled radiance L is a function of the geometric conditions, Ω (sun and satellite zenith angles and the sun-satellite relative azimuth angle) and the surface and atmospheric conditions χ, both of which change with observation time and location. In practice this integral is determined numerically and replaced with a summation.

$$\tilde{L}_{\mathrm{TOA};t,i,j} = \sum_{\lambda_k=\lambda_{\min}}^{\lambda_{\max}} \xi_t(\lambda_k;t) L\left(\lambda_k;\Omega_{t,i,j},\chi_{t,i,j}\right)\delta\lambda_k + 0\,. \qquad \textit{Eq 3-7}$$

Here the 0 represents the appropriateness of this numerical integration.

3.2.3 Spectral response function

The normalised (to peak 1) spectral response function $\xi_t(\lambda;t)$ has been determined for this project also using reference sites whose radiance is determined from radiative transfer functions, and also Eq 3-7. While the radiometric gain term is determined from two types of reference site (several desert and ocean sites), three types of reference site are used to estimate the spectral response function (one desert site, ocean sites and deep convective clouds). The method to determine the spectral response function is described in detail in [Quast and Giering, 2016].

The spectral response function is modelled by a linear combination of Bernstein basis polynomials combined with a degradation model that defines a temporal drift of the spectral response function, with a stronger degradation for short wavelengths than for longer wavelengths. The linear combination is established to minimise the differences between the measured and radiative transfer modelled radiances over the three types of test site. This linear combination changes as a function of time as the instrument degrades.

3.2.4 Zero

The term zero in the expression $(a_0 + a_1 D_t + 0)$ comes from the following effects:

- The suitability of $a_0 + a_1 D_t$ as obtained from the reference sites to represent the true instantaneous instrument gain. For example the annual cycle of the satellite interior temperature induces an annual cycle of the responsivity of the sensor. Therefore there are seasonal patterns to the residuals to this straight line fit.

- The assumption in the measurement equation that the instrument is linear in Earth counts

3.3 Measurement Function Diagram

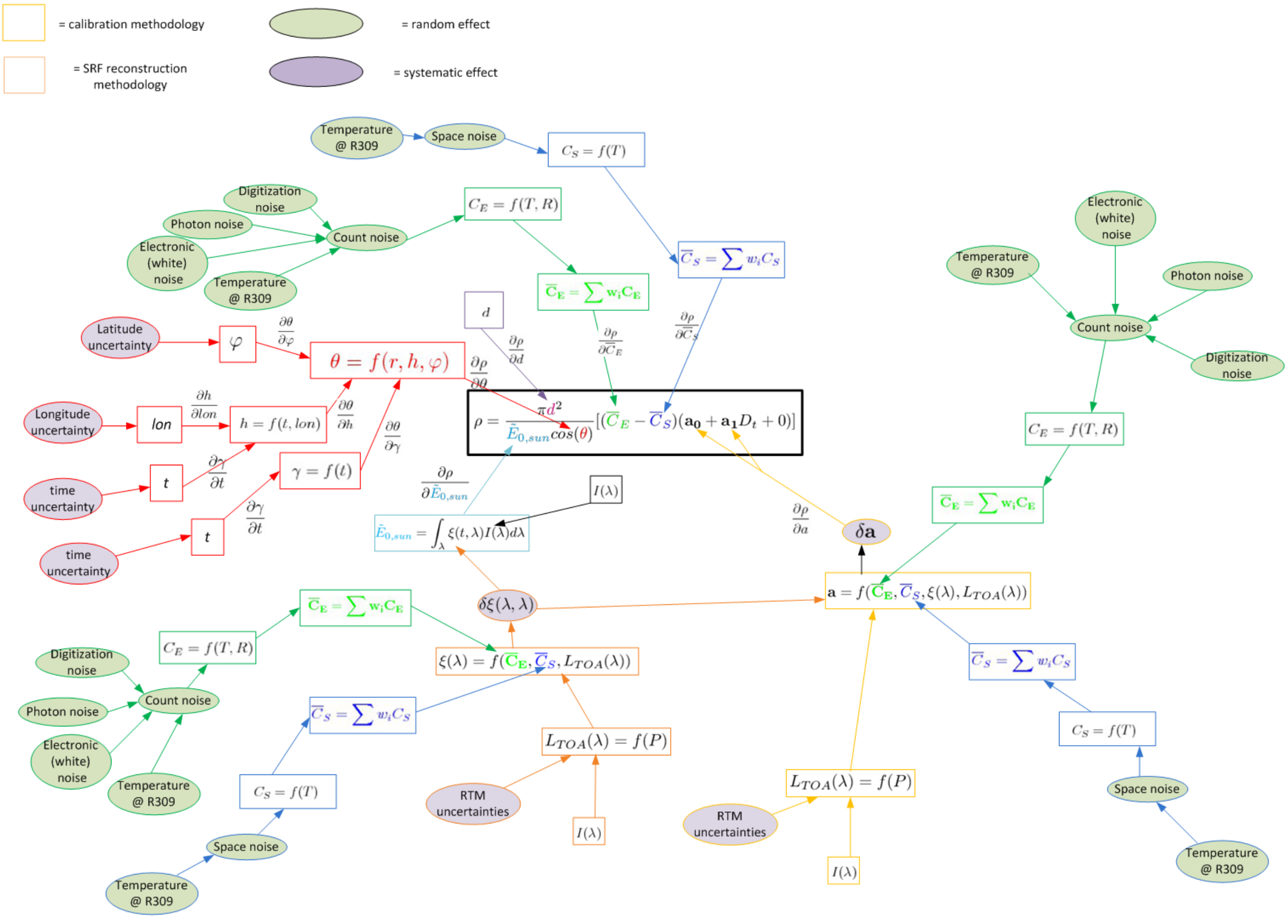

Figure 3 Measurement function diagram for MVIRI

4 A discussion of different terms

In this section we consider the different sources of uncertainty and discuss the error correlation structure for each effect in the different dimensions using the Effects Tables that have been described in D2-2a.

4.1 Noise in Earth Counts and Space Counts

Earth pixel counts in georectified images are interpolated values. This reflects the fact that the pixels in the rectified grid have modified locations. The interpolation is a cubic spline, using the 4 × 4 closest non-rectified pixels. This results in correlations of the errors within this pixel range. Since a spline involves a weighted average, this is treated as a truncated-Gaussian correlation structure.

The space-count value is taken by averaging all four space corners for both individual detectors (=in total 8 space corners are evaluated) to get a single dark signal applied throughout the image, despite the fact that the noise levels of the two detectors are different. In the georectification of the Earth image, data from both individual detectors is combined, and for different pixels there is a different relative weighting of the two detectors. The single image dark count is subtracted from this georectified Earth count.

Because a single space count value is used for all pixels, there are two possible correlation structures for the space count error. If the dominant uncertainty is in the estimation of the dark count from the space corners, then this would be a fully systematic effect. On the other hand, if the dominant uncertainty is the representativeness of the dark count determined from the space corners to the actual dark count for an individual measurement, then this would be a random effect. We consider this a random effect and that it has a magnitude equal to the Allan deviation of the space corners (not reduced by averaging of the space corners since it is dominated by representativeness, it is, however, reduced by the georectification spline fit).

The noise in the Earth counts is determined by combining the uncertainties associated with white noise and digitisation noise. The white noise is estimated either from inverse modelling (for uniform scenes) or from the Allan deviation of the space corner counts. The digitisation noise is the standard deviation of a uniform (rectangular) distribution with a half width of 0.5 counts. Our evaluation of the photon shot noise, a source of noise common for optical instruments, has revealed that it is below 5.4×10^{-9} counts and therefore insignificant. The combined earth count noise thus is:

$$u(C_{\mathrm{E}}) = \sqrt{u^2\left(C_{\mathrm{E,wh}}\right) + u^2\left(C_{\mathrm{E,Dig}}\right)}$$ *Eq 4-1*

Table 1 Effects tables for the Earth, averaged-Space and averaged-IWCT counts

Table descriptor			
Name of effect		Earth Count Noise	Averaged space count noise
Affected term in measurement function		C_{E}	$\bar{C}_{\mathrm{S}}$
Instruments in the series affected		All	All
Correlation type and form	**Pixel-to-pixel [pixels]**	Bell shaped	Bell shaped
	from scanline to scanline [scanlines]	Bell shaped	Bell shaped
	between images [images]	Random	Random
	Between orbits [orbit]	N/A	N/A
	Over time [time]	Random	
Correlation scale	**Pixel-to-pixel [pixels]**	[n=5]	[n=5]
	from scanline to scanline [scanlines]	[n=5]	[n=5]
	between images [images]	[0]	[0]
	Between orbits [orbit]	N/A	N/A
	Over time [time]	[0]	[0]
Channels/bands	**List of channels / bands affected**	N/A	N/A
	Correlation coefficient matrix	N/A	N/A
Uncertainty	**PDF shape**	Digitised Gaussian	Digitised Gaussian

	units	Counts	Counts
	magnitude	Provided per pixel, Eq 4-1	Provided per pixel, from Allan variance
Sensitivity coefficient		$\frac{\partial\rho}{\partial\bar{C}_\mathrm{E}}$, Eq 4-2	$\frac{\partial\rho}{\partial\bar{C}_\mathrm{S}}$, Eq 4-3

The sensitivity coefficients can be determined as the first derivatives of the measurement equation (middle term) or as the relative sensitivity by dividing both sides by reflectance (right term):

$$\frac{\partial\rho}{\partial\bar{C}_\mathrm{E}} = \frac{\pi d^2}{\tilde{E}_{0,\mathrm{sun}}\cos\theta}\left(a_0 + a_1 D_t\right) = \frac{\rho}{\left(\bar{C}_\mathrm{E} - \bar{C}_\mathrm{S}\right)} \quad \textit{Eq 4-2}$$

$$\frac{\partial\rho}{\partial\bar{C}_\mathrm{S}} = \frac{-\pi d^2}{\tilde{E}_{0,\mathrm{sun}}\cos\theta}\left(a_0 + a_1 D_t\right) = \frac{-\rho}{\left(\bar{C}_\mathrm{E} - \bar{C}_\mathrm{S}\right)} \quad \textit{Eq 4-3}$$

4.2 Spectral response function, band-integrated solar irradiance

The spectral response function (SRF) is determined through a minimisation routine which minimises the differences between the modelled and measured top-of-atmosphere reflectance values over different calibration reference sites. The SRF is provided to EUMETSAT for processing the FCDR as a tabulated list of values at different wavelengths, along with a covariance matrix which provides the covariance associated with the different wavelength pairs. Note that because of the fitting process there is significant correlation between the SRF values for different wavelengths.

The SRF is used to determine the band-integrated solar spectral irradiance using a discretised version of Eq 3-2:

$$\tilde{E}_{0,sun} = \sum_i \xi(\lambda_i) E_{0,sun}(\lambda_i)\delta\lambda_i + 0 \quad \textit{Eq 4-4}$$

Note that we consider the uncertainty associated with the band-integrated solar irradiance to be dominated by the uncertainty associated with the SRF. Uncertainties associated with the solar spectral model are small and minimised when the same model is used for the calibration sites.

The Plus Zero term in Eq 4-4 represents the extent to which the summation is an approximation to the original integral. We have tested the sensitivity of this summation to the wavelength spacing used and it is insignificant, therefore we consider the uncertainty associated with the plus zero term to be negligible.

The SRF is also used in the gain calibration, using Eq 3-7.

Because it is used in both of these, there is an error correlation between the solar irradiance and the calibration coefficients in the measurement function which must be considered in uncertainty propagation. This has not yet been fully considered.

The SRF varies with time, but this variation is defined explicitly by the degradation model. The errors in the SRF are therefore fully correlated across time, with a sensitivity coefficient defined by the degradation model.

Table 2 Effects tables for the SRF

Table descriptor			
Name of effect		Spectral response function effect on solar irradiance	Spectral response function effect on calibration
Affected term in measurement function		$\tilde{E}_{0,\mathrm{sun}}$	$[a_0 \quad a_1]$
Instruments in the series affected		All	All
Correlation type and form	**Pixel-to-pixel [pixels]**	Rectangular_absolute	Rectangular_absolute
	from scanline to scanline [scanlines]	Rectangular_absolute	Rectangular_absolute
	between images [images]	Rectangular_absolute	Rectangular_absolute
	Between orbits [orbit]	N/A	N/A
	Over time [time]	Rectangular_absolute	Rectangular_absolute
Correlation scale	**Pixel-to-pixel [pixels]**	$[-\infty, +\infty]$	$[-\infty, +\infty]$
	from scanline to scanline [scanlines]	$[-\infty, +\infty]$	$[-\infty, +\infty]$
	between images [images]	$[-\infty, +\infty]$	$[-\infty, +\infty]$
	Between orbits [orbit]	N/A	N/A
	Over time [time]	$[-\infty, +\infty]$	$[-\infty, +\infty]$
Channels/bands	**List of channels / bands affected**	N/A	N/A
	Correlation coefficient matrix	N/A	N/A
Uncertainty	**PDF shape**	Gaussian	Gaussian
	units	W m^{-2}	
	magnitude	?	?
Sensitivity coefficient		Not yet determined	

4.3 Earth-sun distance

The maximum error of the Earth-sun distance d, calculated using the VSOP87 (French: Variations Séculaires des Orbites Planétaires; Bretagnon and Francou, 1988) concept, is one arcsecond, equalling around 725281 m. The sensitivity coefficient of d can be written as:

$$\frac{\partial\rho}{\partial d} = \frac{2\pi(C_{\mathrm{E}} - C_{\mathrm{S}}(a_1 D_{\mathrm{t}} + 0 + a_0)d}{E_0 \cos(\theta)} \qquad \text{Eq 4-5}$$

An example typical measurement could be:

C_{E}	50
C_{S}	5

a_0	0.92
a_1	0
D_t	1
d	1
E_0	690 [W m^{-2}]
θ	0.44 [radians]

For this scenario an uncertainty of 725281 m (4.85×10^{-6} AU) would have an impact of only 1.99×10^{-6} reflectance points (= 0.0009 % of the BRF value of 0.208). Therefore we consider d a negligible uncertainty effect.

4.4 Solar zenith angle

The solar zenith angle is calculated using Eq 3-5 from the longitude, latitude and acquisition time. Maximum uncertainty of the acquisition time is around 30 seconds. For acquisition time variations of this order, the SZA has a sensitivity close to zero. Therefore we consider it to be a negligible uncertainty effect. Uncertainties associated with longitude and latitude have been analysed by looking at errors in the positioning of ground landmarks. The results show that landmark errors in longitude direction can be assumed to be correlated across 50 lines and pixels, while those in latitude direction are correlated across 1000 pixels and 200 lines (Figure 4 and Figure 5 in Appendix A). There is no significant autocorrelation in the landmark errors, and therefore the temporal error correlation form and error correlation form between images is random.

Table 3 Effects tables for the Solar Zenith Angle

Table descriptor			
Name of effect		Longitude	Latitude
Affected term in measurement function		θ	θ
Instruments in the series affected		All	All
Correlation type and form	**Pixel-to-pixel [pixels]**	Bell-shaped	Bell-shaped
	from scanline to scanline [scanlines]	Bell-shaped	Bell-shaped
	between images [images]	Random	Random
	Between orbits [orbit]	N/A	N/A
	Over time [time]	Random	Random
Correlation scale	**Pixel-to-pixel [pixels]**	[-50,+50]	[-1000,+1000]
	from scanline to scanline [scanlines]	[-50,+50]	[-200,+200]
	between images [images]	[0]	[0]
	Between orbits	N/A	N/A

	[orbit]		
	Over time [time]	[0]	[0]
Channels/bands	**List of channels / bands affected**	N/A	N/A
	Correlation coefficient matrix	N/A	N/A
Uncertainty	**PDF shape**	Gaussian	Gaussian
	units	Degrees	Degrees
	magnitude	Provided per pixel	Provided per pixel
Sensitivity coefficient		$\frac{\partial\rho}{\partial lon}=\frac{\partial\rho}{\partial\theta}\frac{\partial\theta}{\partial h}\frac{\partial h}{\partial lon}$, Eq 4-6, Eq 4-7, Eq 4-7	$\frac{\partial\rho}{\partial\varphi}=\frac{\partial\rho}{\partial\theta}\frac{\partial\theta}{\partial\varphi}$, Eq 4-6, Eq 4-8

The sensitivity coefficients are:

$$\frac{\partial\rho}{\partial\theta}=\frac{\pi d^2}{\tilde{E}_{0,\mathrm{sun}}\cos^2\theta}\left[\left(\bar{C}_{\mathrm{E}}-\bar{C}_{\mathrm{S}}\right)\left(a_0+a_1D_t+0\right)\right]\frac{\sin\theta}{\cos^2\theta}=\rho\tan\theta\,. \tag{Eq 4-6}$$

$$\frac{\partial\theta}{\partial h}=\frac{\cos(\gamma)\cos(\varphi)\sin(h)}{\sqrt{1-\left(\sin(\gamma)\sin(\varphi)+\cos(\gamma)\cos(h)\cos(\varphi)\right)^2}}\,. \tag{Eq 4-7}$$

$\frac{\partial\rho}{\partial lon}$ → determined using Monte-Carlo and provided inside the FCDR LUT – file [Roebeling et al. 2017] *Eq 4-7*

$$\frac{\partial\theta}{\partial\varphi}=-\frac{\sin(\gamma)\cos(\varphi)-\cos(\gamma)\cos(h)\sin(\varphi)}{\sqrt{1-\left(\sin(\gamma)\sin(\varphi)+\cos(\gamma)\cos(h)\cos(\varphi)\right)^2}} \tag{Eq 4-8}$$

5 Calibration coefficients (harmonisation)

Unlike the other FIDUCEO FCDRs, there is not a direct harmonisation using matchups to a reference sensor. However, the determination of the calibration coefficients, a_0, a_1 shares much in common with the process of harmonisation. The calibration coefficients are determined by fitting a model (a straight line model) to results obtained by comparing the sensor measured radiance to that of a reference, here a modelled spectrally-integrated TOA radiance value for several desert and several ocean sites. The fit is illustrated in Figure 6 in the appendix.

From the calibration process we obtain the uncertainties associated with a_0 and a_1 and the covariance between them. The errors in these terms are constant for the whole sensor. The term +0 in the main measurement function, Eq 3-1, represents the extent to which the linear calibration equation applies to the whole sensor. In practice, when the residual is plotted over time a seasonal effect is seen (Figure 7, appendix).

This can come from three effects:

- A responsivity effect due to satellite warming or cooling. The exposition of a geostationary satellite to the sun changes with a yearly cycle, affecting the thermal environment inside the spacecraft. The sensitivity of a silicon photodiode in turn changes with the temperature of the material. Since the silicon responsivity increases with temperatures, the calibration coefficients in the presence of high temperatures (usually winter) need to be smaller. This is a real seasonal effect that needs to be accounted for in the uncertainty analysis.
- An impact of the seasonal cycle of the satellite temperature on the noise level. Generally, electronics noise (white noise) increases with the temperature of an electronic assembly. In MVIRI instruments this effect is masked by a thermal behaviour of the A/D converters. This behaviour superimposes an artificial seasonal cycle of the dark-signal and of its noise level. However, the increasing noise level of the dark signal sufficiently covers the effect of the artificially increased dark signal (Figure 8, appendix).
- An effect due to errors in the radiative transfer model’s determination of the TOA reflectance over the sites due to an increased sensitivity to SZA (which have a significant uncertainty) and inaccuracies in the BRF model of the site which provide a seasonal variation. This would be an artificial effect that will not affect the trend.

It is likely that the majority of the observed deviation is due to the latter effect and therefore the errors in the model (the zero term) are considered to be smaller than the observed variation. They are, however, considered fully systematic.

Table descriptor			
Name of effect		Harmonisation coefficients	Plus Zero
Affected term in measurement function		$[a_0 \quad a_1]$	$+0$
Instruments in the series affected		All	All
Correlation type and form	**Pixel-to-pixel [pixels]**	Rectangular_absolute	Rectangular_absolute
	from scanline to scanline [scanlines]	Rectangular_absolute	Rectangular_absolute
	between images [images]	Rectangular_absolute	Rectangular_absolute
	Between orbits [orbit]	N/A	N/A
	Over time [time]	Rectangular_absolute	Rectangular_absolute
Correlation scale	**Pixel-to-pixel [pixels]**	$[-\infty,+\infty]$	$[-\infty,+\infty]$
	from scanline to scanline [scanlines]	$[-\infty,+\infty]$	$[-\infty,+\infty]$
	between images [images]	$[-\infty,+\infty]$	$[-\infty,+\infty]$
	Between orbits [orbit]	N/A	N/A
	Over time [time]	$[-\infty,+\infty]$	$[-\infty,+\infty]$
Channels/bands	**List of channels / bands affected**	N/A	N/A

	Correlation coefficient matrix	N/A	N/A
	Covariance	N/A	N/A
Uncertainty	**PDF shape**	Gaussian	Gaussian
	units	Units of $\left[a_0 \quad a_1\right]$ [W m-2 sr-1 /DC Year W m-2 sr-1 / DC]	Units of a0
	magnitude	Covariance matrix	
Sensitivity coefficient		$\frac{\partial\rho}{\partial a_0},\frac{\partial\rho}{\partial a_1}$,Eq 5-1, Eq 5-2	

$$\frac{\partial\rho}{\partial a_0}=\frac{d^2\pi(C_{\mathrm{E}}-C_{\mathrm{S}})}{\tilde{E}_{0,\mathrm{sun}}\cos(\theta)}$$

Eq 5-1

$$\frac{\partial\rho}{\partial a_1}=\frac{d^2\pi(C_{\mathrm{E}}-C_{\mathrm{S}})D_{\mathrm{t}}}{\tilde{E}_{0,\mathrm{sun}}\cos(\theta)}$$

Eq 5-2

A Appendix on detailed information about uncertainty components

A.1 Error correlation in longitude and latitude from landmark analysis

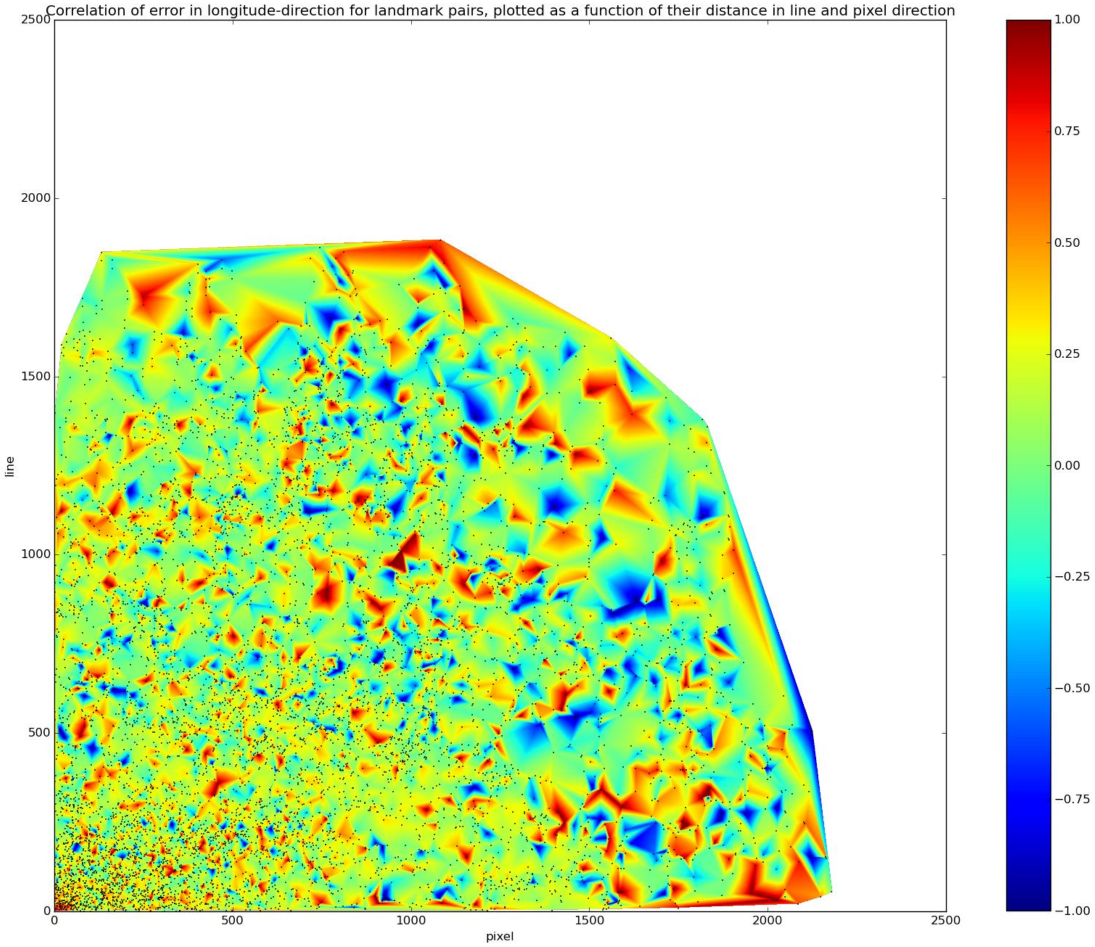

Figure 4: Correlation of landmark errors across all landmark pairs in longitude direction, plotted as a function of their distance in pixel- and line-direction. Landmark errors can be strongly negatively or positively correlated even if they have large distances. However, landmarks with distances of up to 50 pixels are commonly positively correlated (lower left corner).

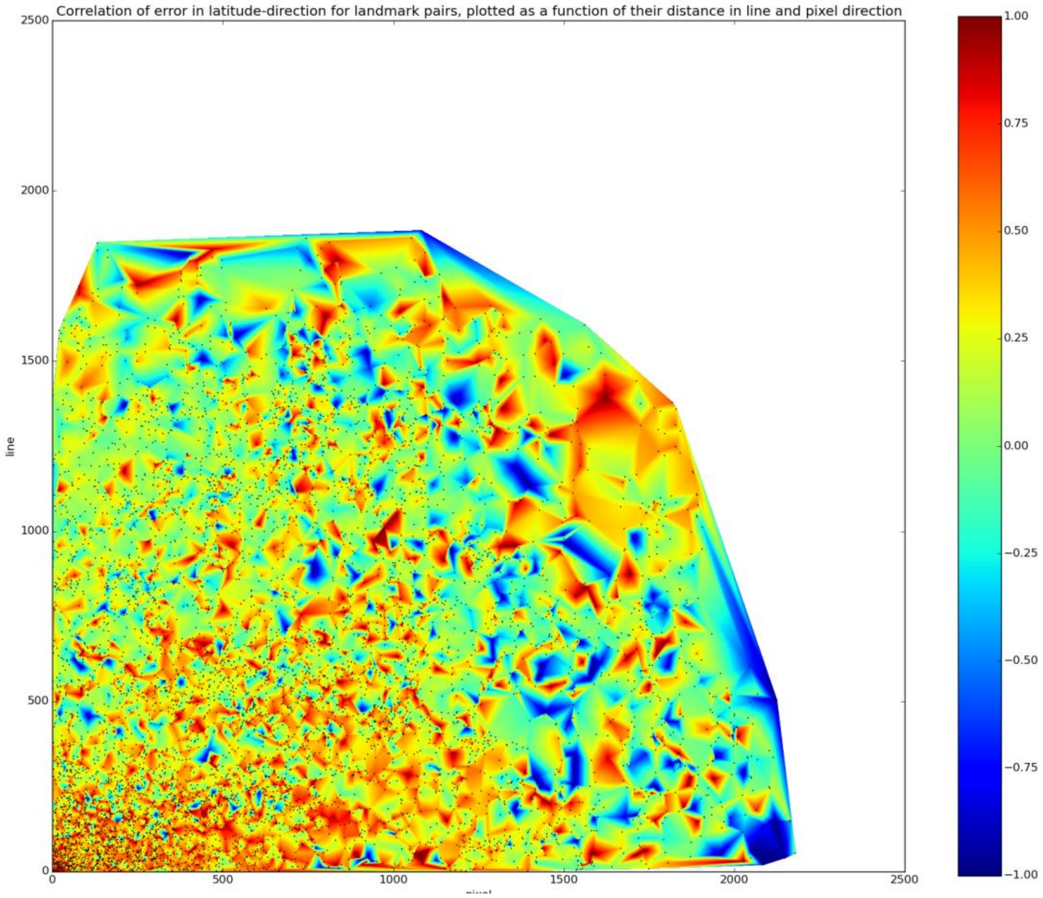

Figure 5: Correlation of landmark errors across all landmark pairs in latitude direction, plotted as a function of their distance in pixel- and line-direction. Landmark errors can be strongly negatively or positively correlated even if they have large distances. However, landmarks with distances of up to 200 pixels in line direction or 1000 pixels in pixel direction are commonly positively correlated (lower left corner, stretching towards the lower right corner).

A.2 Straight line fit of harmonisation coefficients from reference sites

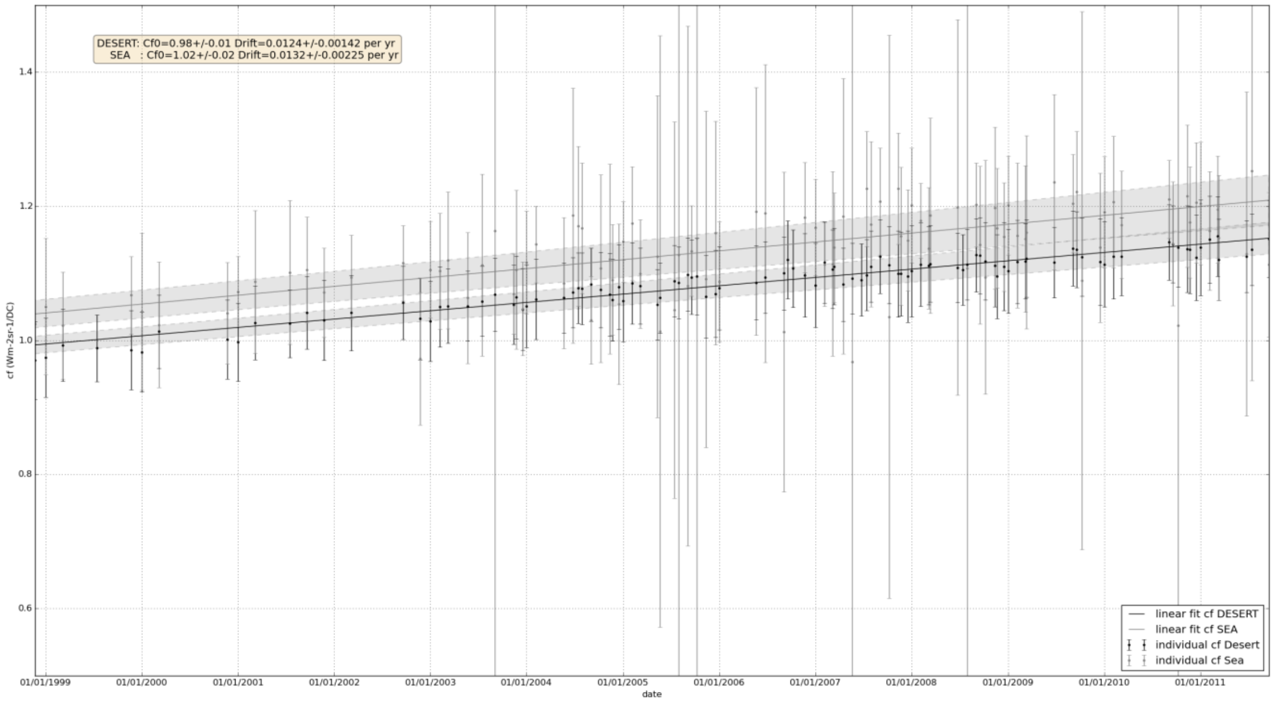

Figure 6: Illustration of the straight line model that is fitted to 5-day calibration results obtained by comparing the sensor measured radiance to that of a reference. Note the comparable drift rates above the two different target types, indicating that spectral degradation of the sensor is properly accounted for.

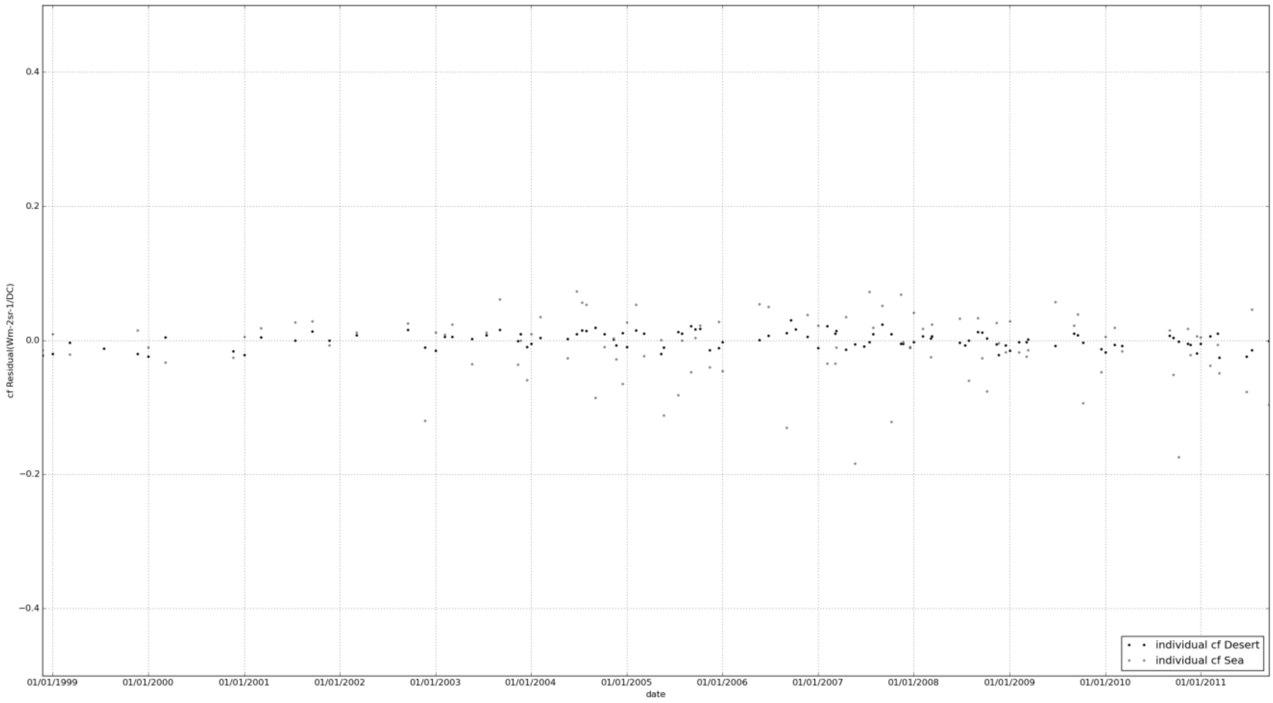

Figure 7: Residuals from the linear fit shown in the Figure above.

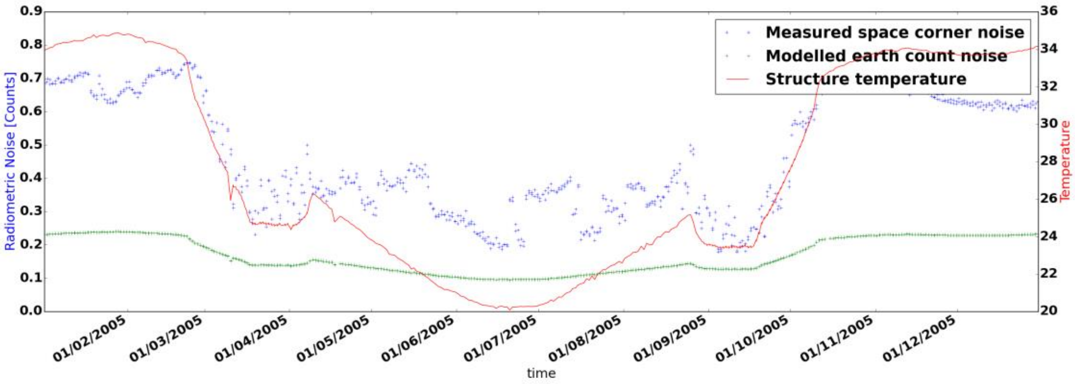

Figure 8: Measured noise of the dark signal (blue) compared to the structure temperature (red) and the modelled electronics noise. Note, that the difference between modelled (expected) electronics noise and measured noise is due to the temperature dependent behaviour of the A/D converter count-switches.